Coordination controlled electrodeposition and patterning of layers of palladium/copper nanoparticles on top of a self-assembled monolayer

She, Zhe; Yao, Zhen; Ménard, Hervé; Tobish, Sven; Lahaye, Dorothée; Champness, Neil R.

Published in:
Nanoscale

DOI:
10.1039/C9NR03927A

Publication date:
2019

Document Version
Peer reviewed version

Coordination Controlled Electrodeposition and Patterning of Layers of Palladium/Copper Nanoparticles on Top of a Self-Assembled Monolayer

Zhe She[1†], Zhen Yao[1], Hervé Ménard[2], Sven Tobish[3], Dorothée Lahaye[4], Neil R. Champness[4], Manfred Buck[1]*

[1]EaStCHEM School of Chemistry, University of St. Andrews, North Haugh, St. Andrews, KY16 9ST, U.K.

[2]Leverhulme Research Centre for Forensic Science, University of Dundee, Dundee, DD1 4HN, U.K

[3]Drochaid Research Services, North Haugh, St. Andrews, KY16 9ST, U.K.

[4] School of Chemistry, University of Nottingham, University Park, Nottingham, NG7 2RD, U.K.

[†]Present address: Department of Chemistry, Queen's University, 90 Bader Lane, Kingston, K7L 3N6, Canada

ABSTRACT: A scheme for the generation of bimetallic nanoparticles is presented which combines electrodeposition of one type of metal, coordinated to a self-assembled monolayer (SAM), with another metal deposited from the bulk electrolyte. In this way PdCu nanoparticles are generated by initial complexation of Pd^{2+} to a SAM of 3-(4-(pyridine-4-yl)phenyl)propane-1-thiol (PyP3) on Au/mica and subsequent reduction in an acidic aqueous $CuSO_4$ electrolyte. Cyclic voltammetry reveals that the onset of Cu deposition is triggered by Pd reduction. Scanning tunneling microscopy (STM) shows that layers of connected particles are formed with an average thickness of less than 3 nm and lateral dimensions of particles in the range of 2 to 5 nm. In X-ray photoelectron spectra a range of binding energies for the Pd 3d signal is observed whereas the Cu 2p signal appears at a single binding energy, even though chemically different Cu species are present: normal and more noble Cu. Up to three components are seen in the N 1s signal, one originating from protonated pyridine moieties, the others reflecting the SAM-metal interaction. It is suggested that the coordination controlled electrodeposition yields layers of particles composed of a Pd core and a Cu shell with a transition region of a PdCu alloy. Deposited on top of the PyP3 SAM, the PdCu particles exhibit weak adhesion which is exploited for patterning by selective removal of particles employing scanning probe techniques. The potential for patterning down to the sub-10 nm scale is demonstrated. Harnessing the deposition contrast between native and PdCu loaded PyP3 SAMs, structures thus created can be developed into patterned continuous layers.

INTRODUCTION

Among the many applications of self-assembled monolayers for surface modification and patterning,[1-4] templated electrodeposition is one where a combination of interfacial properties, encompassing charge transfer, interfacial energy and chemical functionality, is harnessed for the generation of metal structures.[5, 6]

There are two distinctly different approaches to controlling electrodeposition using SAMs. One, more commonly employed, strategy is illustrated in Figure 1a. The method is based on SAMs which render an electrode electrochemically passive, thus, confining deposition to SAM free areas or defects in the SAM.[7-16] In the latter case, deposition starts at the SAM/electrode interface and proceeds via a mushroom type growth.[9, 10, 17] The nature of these defects can be very local and intrinsic to the native SAM such as structural defects and packing faults or extrinsic to the SAM originating from contaminations or intentionally introduced by patterning techniques.[7, 18] Notably, for aromatic SAMs intrinsic defects acting as nucleation sites can be eliminated by electron beam induced cross-linking of the molecules whereas aliphatic SAMs undergo damage. Consequently, deposition occurs in areas of either the native (negative resist) or irradiated (positive resist) layer. The high spatial resolution of e-beam lithography, enabling patterning of SAMs down to the sub-20 nm range,[19] makes SAM controlled electrodeposition also of interest for the generation of metallic nanostructures.[7, 10, 12, 20, 21] However, even though defect mediated deposition allows the generation of structures on the nanometer scale,[7, 10, 12, 20, 21] the statistical nature of defects and dynamic processes in SAMs at defects such as diffusion of molecules will limit the level of control over nucleation and, therefore, the accuracy of the deposition process.

For this reason the second, much less explored deposition scheme is of interest as it relies on the chemical functionality of SAM molecules, thus promising a more active control of the deposition process. The key point is the electrochemical reduction of ions coordinated to a SAM which, similar to protocols where reduction is accomplished chemically,[22-25] follows a complexation step without potential control as illustrated in Figure 1b. The specific features of this coordination controlled electrodeposition (CCED) scheme are that (i) the amount deposited is defined by the SAM through the number of coordination sites, (ii) the metal clusters formed are localized on top of the SAM, and (iii) the potential provides a precisely adjustable parameter for controlling the deposition kinetics. Originally performed in an electrolyte free of reactive species[26] (route A), this scheme has been modified and extended in various ways including the combination of electrochemical and electroless deposition.[24, 25, 27-42] In this context it is also worth noting that such a two step procedure of fixation of metal ion complexes and electroreduction in a non-reactive elec-

trolyte has also been applied to generate metal nanoparticles on monolayer grafted carbon nanotubes or imbedded in layer by layer grown polymer films.[43-45]

One variant of the complexation-reduction scheme, particularly important to the work presented below, is that the ions coordinated to the SAM can be reduced in the presence of metal ions in the bulk electrolyte (Figure 1b, route B) using SAMs which exhibit the structural quality to suppress defect mediated deposition from the bulk electrolyte. This not only simplifies the two step process of complexation and reduction of the coordinated ions to a one pot procedure but also makes multiple complexation-deposition cycles straightforward.[25, 31] However, this approach offers the additional option of combining deposition from species coordinated to the SAM and present in the bulk electrolyte. This does not only overcome the limitation of a purely coordination mediated deposition with respect to the amount deposited but also provides unexplored ways for binary metal deposition if both a coordinating metal and a non-coordinating metal are present as illustrated by route B of Figure 1b.

Exploring the scope of the CCED scheme for the generation of metal nanostructures, the present paper focuses on the combination of 2D/3D deposition and the opportunities arising for nanoscale patterning. Using a pyridine terminated SAM and the established molecular design of a combination of an aromatic moiety with a short aliphatic spacer chain which yields structurally well-defined SAMs,[46, 47] the codeposition of Pd coordinated to the SAM and Cu from the bulk electrolyte is investigated.

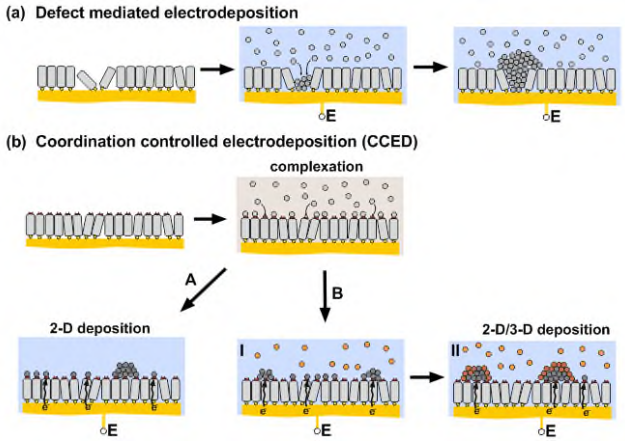

Figure 1: Schemes of SAM controlled electrodeposition processes, illustrating deposition at defects of a chemically passive SAM (a) or on top of a chemically reactive coordinating SAM (b). In the CCED scheme route A denotes deposition of only coordinated species in an inert electrolyte whereas B includes deposition of species from the bulk electrolyte with reduction of coordinated species (I) preceding deposition from the bulk (II). E indicates electrochemically controlled steps

MATERIALS AND METHODS

Materials and sample preparation. Potassium hydroxide (Fluka, p.a.), palladium sulfate (Fluka, 99.995%), sulfuric acid (Sigma-Aldrich, 99.999%), and copper sulfate pentahydrate (Sigma-Aldrich, 99.995%) were used as purchased. Platinum wires (diameter of 0.25 mm) and copper wire (diameter of 0.25 mm) used as reference and counter electrodes, and Pt/Ir (80:20, diameter of 0.25 mm) wire for STM tips were purchased from ADVENT Research Materials. The synthesis of PyP3 has been described previously.[48] Substrates, 300 nm thick epitaxial Au(111) films grown on mica (Georg Albert PVD, Silz Germany), were stored in vacuum and flame-annealed prior to SAM modification.

Substrates were cut to size, flame annealed and then immersed into a solution of 250 µM PyP3[48] in a basic ethanol solution (KOH, pH < 10) at 298 K for 12 hours, then rinsed with pure EtOH and blown dry with N_2 gas.

For Pd^{2+} complexation the PyP3/Au/mica sample was immersed in a palladium solution (100 µM $PdSO_4$ in 50 mM aq. H_2SO_4) for 20 mins at room temperature followed by rinsing with dilute H_2SO_4 (pH ~1) and blown dry with N_2 gas.

Electrochemistry. Two types of electrolytes were used in the experiments. For Pd-only deposition pure sulfuric acid (pH~1) was used. Pd/Cu deposition was performed in acidic copper sulfate solutions (aq. H_2SO_4, pH~1) of varying concentrations as stated in the relevant sections. Depositions were performed in home-built small volume cells (3-5 ml), one consisting of a cylindrical KEL-F body with a central stepped bore of 5 and 7 mm in diameter. The substrate was pressed against the bottom of the cell using a viton ring as seal. This cell allowed the experiments to be carried out in a protected atmosphere by purging the electrolyte with N_2 gas for 20 mins prior to and continuously during the experiments.

Care was taken that, in order to minimise dissolution of copper in the case of the Pd/Cu system, samples were removed from the cell after electrodeposition within a few seconds and then immediately blown dry with N_2 gas before rinsing with deionised water and being dried again. Depositions onto AFM patterned Pd/Cu layers were performed in an open cell. Similar to a hanging meniscus configuration the sample was held upside down and then brought into contact with the electrolyte. Pt and Cu wires were used as reference and counter electrodes for the Pd-only and Pd/Cu deposition, respectively. To allow for direct comparison between cyclic voltammograms (CVs) with and without Cu, potentials are referenced to the saturated calomel electrode (SCE) using +0.53 V as difference between Pt and SCE in agreement with literature[49] and -0.02 V for Cu calculated from the concentration corrected standard potential.

Nanoparticle Characterisation and Manipulation. A pico SPM (Molecular Imaging) operating in ambient atmosphere was used, employing tips mechanically cut from a 0.25 mm diameter Pt/Ir wire (80:20). Typical values for bias voltage and tunneling current used for imaging were in the range of 0.5 V - 0.8 V and 1.5 – 10 pA. Condition for removing nanoparticles was 0.1 V/250 pA.

Patterning by AFM was also performed in ambient atmosphere using a Nanosurf EasyScan 2 instrument with a silicon cantilever (Budget Sensors ContAl-G, k = 0.2 N/m). A repulsive force of 42 nN and a scan rate of 2 lines/s were applied. Depending on area, the separation between lines varied from 5 to 1.3 nm. Patterned samples after Cu deposition were imaged in tapping mode with a Bruker Dimension Icon AFM (Veeco SNL-10 tips, k = 0.58 N/m). For image analysis and presentation WSxM software was used.[50]

X-ray photoelectron spectroscopy measurements were carried with a Kratos Axis Ultra-DLD photoelectron spectrometer equipped with a monochromatized Al Kα source. Binding energies are referenced to the Au $4f_{7/2}$ peak at a binding energy of 84 eV. Spectra were fitted using Casa-XPS software and employing a Gaussian/Lorentzian product function (GL30). Due to the large Au 4d signal a Shirley background was used for the Pd 3d region whereas linear backgrounds were applied for the N 1s region.

RESULTS AND DISCUSSIONS

CCED of Pd. For reference, electrochemical reduction of Pd^{2+} coordinated to a PyP3 SAM was performed in 50 mM aq. H_2SO_4.

In agreement with earlier work[26, 30, 31, 40] the cyclic voltammograms (Figure 1a) show a cathodic peak at about -0.15 V in the first cycle which is absent in the subsequent one, thus, indicating the irreversible electrodeposition of Pd. Upon reduction, Pd atoms diffuse at the SAM/electrolyte interface and nucleate to yield nanoparticles on top of the SAM. Large scale STM images like the one shown in Fig. 3a show randomly distributed particles at rather low coverage (less than 25% of total area). In agreement with previous work[31] they are located on top of the SAM as evidenced by their poor adhesion which requires low tunneling currents to avoid removal. The nanoparticles are rather uniform in size as seen from the magnified image and the respective height profile displayed in Fig. 3b. We note at this point that caution is required in the interpretation of height (3-4 nm) and width (6-7 nm) due to the influence of the tip size/shape on the image. Since Pd particles on a PyP3 SAM have been characterised previously[31] and our interest was in the density of the Pd particles we did not aim to optimise the tip resolution, in contrast to imaging of the PdCu particles as discussed below.

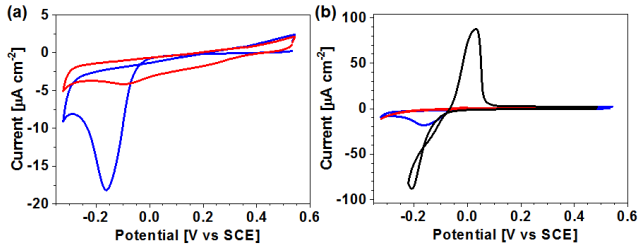

Figure 2. Cyclic voltammograms of metal deposition onto PyP3 modified Au/mica. (a) First (blue curve) and second (red curve) cycles of reduction of Pd^{2+} coordinated to PyP3 in a metal free electrolyte (50 mM H_2SO_4). (b) Deposition in a Cu containing electrolyte (100 µM $CuSO_4$/50 mM H_2SO_4) for a PyP3 SAM with (black curve) and without (red curve) coordinated Pd. For comparison the blue curve of (a) is also shown. Scan rate in all experiments: 10 mV/s.

The deposition process was also monitored by XPS, taking spectra before and after complexation, as well as after Pd reduction. Figures 3c and 3d show the results for the Pd 3d and N 1s regions, respectively, and Table 1 compiles binding energies and line widths of fitted components. For clarity of presentation only the original spectra are shown for the Pd region. An illustrative example of a fit is shown below in Fig. 5b. Since a large Au 4d signal from the substrate superimposes the Pd 3d signal, spectra were recorded at grazing emission angle of the photoelectrons in order to maximize surface sensitivity. The attenuation of the substrate signal is illustrated by spectra of the sample after Pd reduction (orange curves in Figure 3c) taken at emission angles of 0° and 75° with respect to the surface normal. Only a faint shoulder of the $Pd_{1/2}$ signal at 340.6 eV is discernible at normal emission whereas a distinct peak appears at grazing emission.

Compared to the spectrum of the native PyP3 SAM (blue curve) which only shows the Au 4d signal (~353/335 eV) of the substrate, additional peaks are present in the spectrum after exposure of the SAM to the $PdSO_4$ solution (red curve). Separated by 5.26 eV[51] the binding energies of 338.4 eV and 343.7 eV of the Pd doublet are characteristic of Pd^{2+}.[52, 53] A fit yields a rather small linewidth of the $3d_{5/2}$ signal of 1 eV which suggests a well-defined species, i.e., formation of the Pd^{2+}-pyridine complex. It is noted that the line width of the $3d_{3/2}$ component is larger compared to the $3d_{5/2}$ signal as a result of Coster-Kronig broadening.[54] To have a consistent fit procedure this ratio was set to 1.2 for all samples.

After electrochemical reduction (orange curves) the Pd signal appears at significantly lower binding energies, thus, indicating formation of metallic palladium. Due to the shift in binding energy the Pd $3d_{5/2}$ signal coincides now with the Au $4d_{5/2}$ peak which, due to the much smaller line width compared to Au (1.2 eV compared to 3.8 eV), gives this peak a more pointed shape. Repeating the complexation/deposition cycle a few times increases the number of Pd particles[31] which is evident from the comparison of the spectra acquired at 0° emission angle after one cycle (dotted orange curve) and 5 cycles (dotted brown curve).

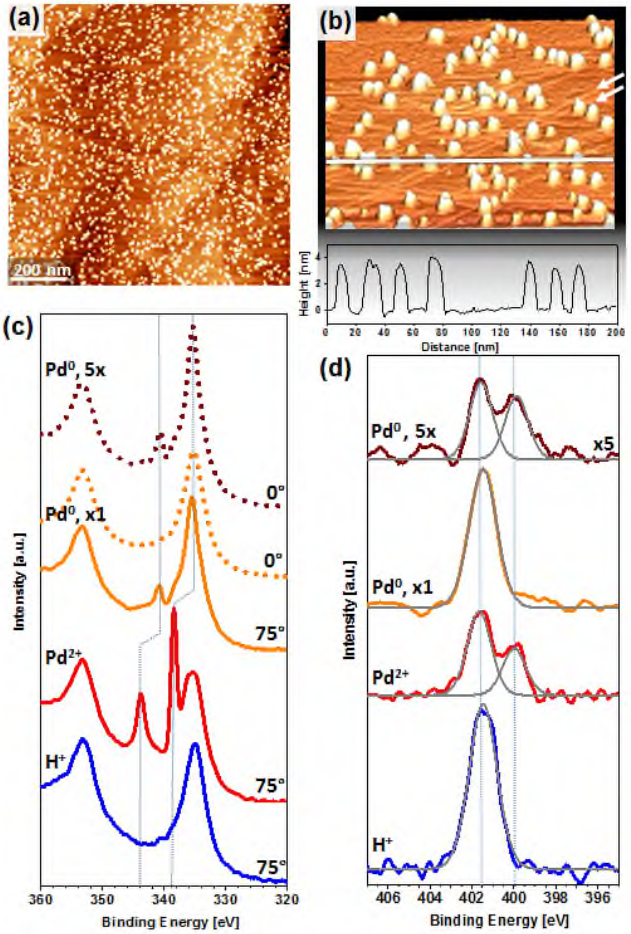

Figure 3. CCED of Pd onto a PyP3 SAM. (a) Large scale STM image in 2D representation. (b) Magnified STM image in 3D representation with height profile along the line shown. Some of the monoatomic substrate steps are marked by white arrows. (U_{tip} = −0.5 V, I = 3 pA) (c,d) XPS spectra at different stages of the CCED process in the Pd 3d (c) and N 1s (d) regions: native SAM after exposure to H_2SO_4 (H^+, blue curves), after Pd complexation (Pd^{2+}, red), after reduction (Pd^0 x1, orange). Top spectra (Pd^0 5x, brown) are from a sample which has undergone 5 complexation/reduction cycles. Solid/dotted curve(s): spectra recorded at an emission angle of 75°/0° from the surface normal. Signal intensity of the top N1s spectrum is multiplied by a factor of 5.

The N 1s spectra parallel the Pd spectra. For the native layer exposed to sulfuric acid (blue curve) a single species at 401.7 eV is observed, indicative of protonated pyridine.[48, 53, 55] After exposure to $PdSO_4$ solution (red curve) a second component at 400 eV is present, indicating the coordination of Pd^{2+} to the pyridine moiety.[53] It is noted that the simultaneous signals from protonated and Pd^{2+} coordinated pyridine reveal a partial complexation (less than 50% in this case) which has also been reported for other pyridine based thiol SAMs.[53, 56] After Pd reduction (orange curve) the second component has disappeared again and the protonated signal has recovered to about the same intensity as before complexa-

tion. Since STM (Fig. 3a,b) clearly shows the presence of Pd nanoparticles the change back to one component after Pd reduction can be explained in two ways. One is that, as suggested in a computational study of a Pd monolayer on a mercaptopyridine SAM,[57] the Pd-pyridine interaction is weak due to adsorbed hydrogen, thus resulting in a reprotonation of the pyridine moieties under the acidic conditions of the experiment. The other one is a simple geometrical argument. As seen from the STM images (Fig. 3a,b) reduction of the Pd^{2+}-ions leads to three dimensional Pd^0-particles at low density which are in contact only with a small fraction of the SAM molecules whereas the large majority of pyridine moieties is exposed to the electrolyte and, therefore, prone to reprotonation. Consequently, the component at 400 eV is very small and could be within the noise of the spectra. The latter interpretation is supported by increasing the number and/or size of clusters through repeated complexation/reduction cycles[31]. After several cycles a second component emerges (brown curve in Fig. 3d) at a binding energy essentially identical to coordinated Pd^{2+}. The intensity of the N 1s signal is now smaller compared to a single deposition due to the significant attenuation of the photoelectrons by metal nanoparticles.

Table 1. Binding energies (BE) and line widths (FWHM) of components in the Pd 3d and N 1s regions. For the $3d_{3/2}$ and $3d_{5/2}$ components of Pd the difference in BE and ratio of line widths were fixed to 5.26 eV and 1.2 eV, respectively. [1]FWHM restricted to minimum of 1 eV.

	Pd $3d_{5/2}$ BE (eV) FWHM (eV)		**N 1s** BE (eV) FWHM (eV)		
PyP3/H^+			401.5 1.55		
PyP3/Pd^{2+}	338.4 1.0		401.7 1.34	400.0 1.34	
PyP3/Pd^0 1 cycle	335.5 1.14		401.5 1.54		
PyP3/Pd^0 5 cycles	335.4 1.29		401.6 1.3	399.9 1.3	
PyP3/CuPd[3]	337.3 1.8	335.9 1.0[1]		400.20 1.22	398.95 1.22
PyP3/CuPd[3] after acid	337.4 1.89	335.9 1.0[1]	401.54 1.33	400.15 1.33	399.02 1.33

Codeposition of coordinated Pd and bulk Cu. As outlined above, CCED in the presence of another metal species in the bulk electrolyte offers interesting prospects for the generation of binary metal structures. The combination of Pd and Cu was chosen as, besides the fact that CuPd alloys are of interest for their catalytic properties[58, 59], Pd^{2+} coordinates to the pyridine moieties at low pH whereas Cu^{2+} does not. First, the effect of Pd-coordination on Cu deposition was examined by cyclic voltammetry. It is evident from Fig. 2b, showing CVs of PyP3 SAMs on Au/mica as prepared and after Pd complexation, that Pd complexation has a pronounced influence on the deposition of Cu from the bulk electrolyte. A PyP3 SAM passivates the electrode, resulting in a gradual onset of the current at values around -0.2 V (red curve) which is a significant cathodic shift compared to clean Au where Cu deposition starts shortly negative of 0 V.[12] As outlined above and illustrated in Fig. 1a, deposition starts at defects in this case.[9, 10, 12] The situation is very different for the PyP3 SAM after Pd complexation as now the current steeply increases at potentials well positive of -0.2 V (black curve). Direct comparison with the CV where Cu is absent (blue curve), reveals a pronouncedly larger cathodic current as well as the presence of an anodic dissolution current, thus, pinpointing the promoting effect of Pd on the deposition of Cu. Notably it also implies that Pd reduction not only precedes but extends well into the range of Cu deposition. This suggests that particles are formed which consist of a Pd core and a Cu shell with, depending on the details of the deposition conditions, a transition region where Pd and Cu are intermixed.

The increase in the amount of deposited metal is fully confirmed by the microscopic characterisation. The STM images shown in Fig. 4 are very different from those without Cu. For the case shown here, deposition was performed by stepping from the open circuit potential (OCP) to -0.16 V and sweep the potential to -0.04 V. While the influence of the deposition conditions on the deposition process will be addressed in detail in a forthcoming publication, the condition chosen here was such that the starting potential was well in the flat part of the CV of the native PyP3 SAM (red curve of Figure 2b), i.e., positive of values where defect mediated Cu deposition through imperfections in the layer could occur. The stopping potential was set to a value just negative of the value where Cu dissolution starts. Under these conditions an essentially continuous layer is formed, in pronounced contrast to the well separated particles when Cu is absent (Figure 3). From the height profile (Figure 4b), which includes a defect in the layer (marked by arrow), a film thickness in the range of 2-2.5 nm is inferred. This is sufficiently thin that, as seen in the large scale image of Fig. 4a, steps in the underlying substrate are still discernible. The higher magnification image (Fig. 4b) reveals that the particle shape and size varies with typical values for the latter in the range of 2-5 nm. Assuming that the measured dimensions reflect the geometry of the particle (care was taken that particle dimensions are not artificially broadened by tip effects) and are not substantially distorted by the influence of electronic effects on the tunneling current, the aspect ratio of the particles of about 2:1 suggests hemisphere-like particles. In combination with the promoting effect of Pd this suggests, that also for Pd-Cu codeposition, the particles are located on top of the SAM. This is very different from the defect mediated Cu deposition on non-coordinating SAMs, where the metal grows out from the substrate in a mushroom-like fashion. One of the consequences of on top deposition is a much lower adhesion of the particles which is exploited in the patterning experiments described in the next section. Concluding from CV and STM data, Cu deposition is greatly promoted by coordinated Pd, resulting in a drastically different density of particles.

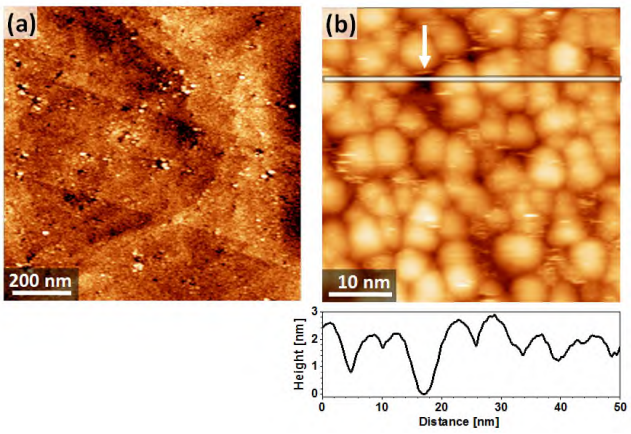

Figure 4. Low (a) and high magnification (b) STM images of codeposition of Pd coordinated to PyP3 SAM and Cu from bulk electrolyte. Deposition was performed in 1 mM $CuSO_4$/50 mM H_2SO_4 electrolyte applying a linear potential sweep from -0.16 V to -0.04 V (vs Cu^{2+}/Cu) at a scan rate of 5 mV/s. Tunneling conditions: U_{tip} = 0.5 V, I = 3 pA.

The Pd assisted Cu deposition was further elucidated by XPS and the respective spectra in the Cu 2p, Pd 3d, and N 1s regions are compiled in Figure 5 which shows two sets of data. Set I comprises spectra of a sample measured after deposition whereas set II is from the same sample after exposure to 50 mM aqueous H_2SO_4. It is noted that the electrodeposition was performed in a nitrogen purged electrolyte under inert gas atmosphere and the time to unmount the sample and remove residual electrolyte was minimised. This is important as for the small amounts of Cu deposited, exposure of the sample to the acidic electrolyte under ambient atmosphere distorts the results as dissolved oxygen in combination with the acidic electrolyte results in the formation of Cu oxide and subsequent dissolution by the acid. In fact this way of Cu dissolution was deliberately applied before acquiring the spectra of set II.

First focusing on the spectra of set I, a clear signature of Cu (binding energies of 932.1 eV and 951.9 eV) is seen which exhibits a 0.6 eV shift to lower binding energies compared to tabulated data of bulk Cu (932.7 eV[51]). The Pd 3d region clearly shows the presence of Pd. However, compared to the Pd-only case (Figure 3c, orange solid curve), the Pd $3d_{3/2}$ component does not exhibit a well-defined peak but extends over a range of more than 2 eV. Fitting the spectra by subtracting a Shirley background, fixing the ratios of the doublet peaks and their line widths, and setting their energy separation to 5.26 eV,[51] the spectrum can be very well described by two Pd $3d_{3/2}$ components at 342.53 eV and 341.13 eV. We stress that this is not to be interpreted as two discrete Pd species but is the minimum of components required for a good fit. In fact, the significantly larger half-width of 2.13 eV of the second peak compared to the corresponding Pd $3d_{3/2}$ peak of the Pd-only samples (1.64 eV, see Table 1) suggests an inhomogeneous broadening of the signal due to a range of Pd species in different electronic or oxidation states.

The N 1s spectrum (curve I in Figure 5c) clearly shows two components located at 400.2 eV and 398.95 eV. Since component 2 at 400.2 eV has essentially the same binding energy as the peak in the Pd-only spectrum after multiple coordination/deposition cycles (Fig. 3d, brown curve), we conclude that this reflects the Pd-pyridine interaction. Accordingly, component 1 at 398.95 eV which is in the region of unmodified or weakly interacting pyridine[48, 55, 60] is allocated to the interaction of nitrogen with Cu. The assignments are in line with UHV experiments on pyridine adsorption on Cu[61], Ni[62] and Pt[63] where binding energies around 398-399 eV and ~400 eV have been assigned to chemisorbed and weakly adsorbed states. A notable difference to the Pd-only deposition is the absence of the protonated pyridine signal at 401.5 eV[48, 53, 60] which means that the number of pyridine moieties exposed to the acidic electrolyte is below detection threshold and, therefore, the whole SAM is covered by metal. This agrees well with the STM images showing a continuous layer of PdCu particles.

After exposure of the PdCu/PyP3 sample to sulfuric acid under ambient conditions where bulk Cu is dissolved (set II) the Cu signal (Fig. 5a), although reduced in intensity, remains significant and at the same binding energy as the sample before acid treatment. The Pd signal (Fig. 5b) remains essentially unchanged (notably the fine structure is still there) whereas in the nitrogen spectrum a third species appears at the position of protonated pyridine. Even though the N 1s signal/noise ratio is rather low, comparison of the spectra of set I and II suggests that the signal of the protonated pyridine emerges at the expense of the component at low binding energy. Combining the information from the different species it can be concluded that (i) Cu is present in chemically different states, identical to and more noble than bulk copper, (ii) component 1 in the N 1s spectra represents the interaction of the pyridine moiety with Cu and (iii) component 2 reflects the Pd-N interaction. The fact that the Cu signal does not disappear indicates that a significant fraction is stabilised by Pd which is in agreement with electrochemical studies of PdCu-alloys.[64] In contrast to codeposition of both Cu and Pd from the bulk electrolyte where a shift of the Cu 2p signal by 0.4 V to lower binding energy was observed,[65] in the present case peak position and width remained unchanged after rinsing with acid, i.e., the dissolvable bulk Cu cannot be differentiated from the stabilised Cu by XPS. The behaviour in the Pd region is somewhat different as, deposition of Cu causes clear changes in binding energy compared to the Pd-only case. On the one hand this is similar to codeposition from bulk electrolyte but, on the other hand, it is also substantially different as the changes in binding energy in the present case are much more pronounced, covering a range of more than 2 eV compared to ~0.5 eV.[65]

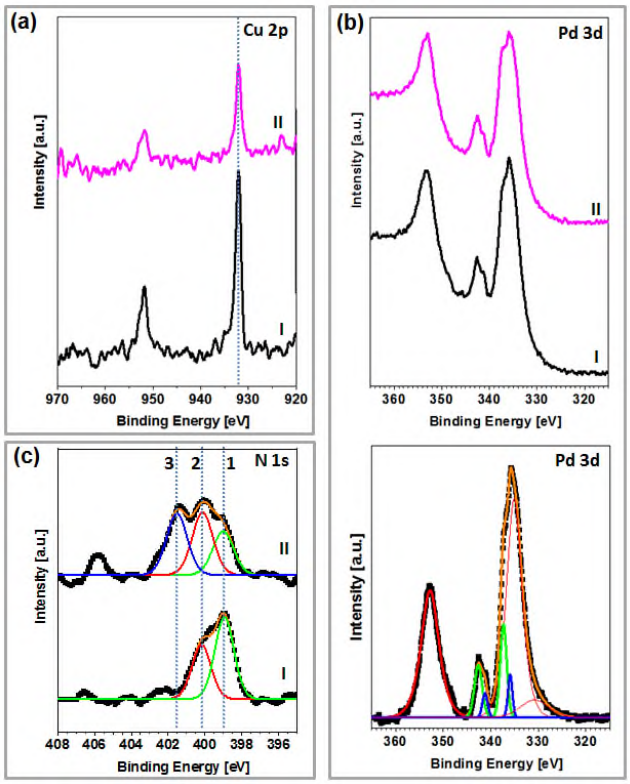

Figure 5. XPS spectra in the Cu 2p (a), Pd 3d (b) and N 1s (c) regions acquired at an emission angle of 75°. Curves I and II denote samples measured after deposition and after rinsing with 50 mM aqueous solution of non-deaerated H_2SO_4, respectively. Bottom panel of (b) and panel (c) show experimental data (black squares) after background subtraction, envelopes (orange curves) and fitted components with doublets in the Pd spectrum in same colour (green/blue). Deposition conditions as in Figure 3.

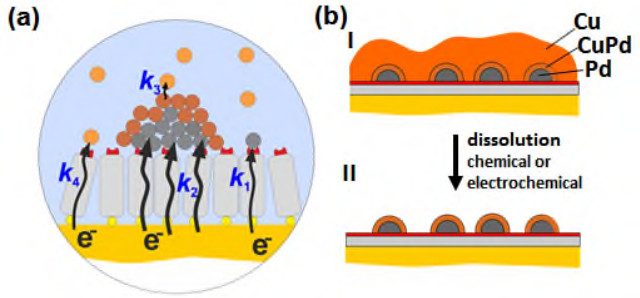

Figure 6. (a) Illustration of electron tunneling pathways in the Pd/Cu deposition processes labelled by their corresponding rate constants k_i. (b) Schematic representation of metal layer after electrodeposition (I), comprised of particles with a Pd/PdCu core shell structure and a cover layer of bulk Cu, and after dissolution of bulk Cu (II).

From CV, STM and XPS data the picture emerges that the coordination controlled deposition of Pd and Cu on top of the SAM involves different phases with Pd reduction preceding deposition of Cu as illustrated by route B in Fig. 1b. For a more detailed analysis of the process, the principle pathways of charge transfer across a nanoparticle covered SAM have to be considered and how these evolve during deposition. As illustrated in Fig. 6a, reduction of ions can proceed along three routes which involve electron tunneling from the substrate to i) coordinated Pd-ions (labelled by rate constant k_1), ii) non-coordinated Cu-ions at the SAM/electrolyte interface (k_4), and iii) the nanoparticle (k_2) followed by the Cu-ion transfer reaction at the nanoparticle/electrolyte interface (k_3). At the potentials applied here, the only pathway available initially is the reduction of coordinated Pd. As pinpointed by the CVs of Fig. 2b there is no Cu^{2+} deposition at this stage, i.e., the corresponding rate constant k_4 is negligibly small compared to k_1. The reduced Pd atoms diffuse and nucleate to form clusters which opens the pathway characterised by rate constants k_2 and k_3. Their values change profoundly as the deposition progresses. Among a complex interplay of electronic, structural and statistical factors,[66-68] the density of states is a crucial one illustrating the changes when the metal deposits evolve from small, molecule-like clusters to nanoparticles with metallic properties.[66,69,70] At an early stage tunneling across the SAM is rate determining whereas at a later stage k_3 becomes rate determining since k_2 increases due to the dominance of the density of states.[66,69-71] It is noted that Coulomb blockade[30, 31] has also to be taken into account, even though at room temperature it should only be relevant for nanoparticles on the order of ~1 nm and below, keeping in mind that the particles are unprotected, i.e., their capacity is larger compared to monolayer protected clusters (MPCs).

Whereas the dominance of k_1 in the early stages of the deposition yields pure Pd particles, formation of a PdCu alloy implies that there is a phase in the deposition process where k_1 and the combination of k_2 and k_3 are in a similar range, thus resulting in an intermediate phase where Cu deposition from the bulk electrolyte onto the Pd particles occurs simultaneously with the reduction of Pd coordinated to the SAM. This is an essential point, e.g. for patterning described in the next section, as this pronouncedly increases the density of particles compared to the Pd-only case where a submonolayer of coordinated Pd yields nanoparticles at low density. After codeposition of Cu and Pd a third phase of pure Cu deposition follows which, as illustrated in Fig. 6b/I, results in a layer with three compositionally different regions comprising separated Pd nanoparticles, a PdCu shell and a bulk Cu phase which links the particles to a continuous layer. Similar to codeposition of Pd and Cu from bulk electrolyte,[58, 65] Cu is pronouncedly more noble in the alloy than as bulk Cu which makes it straightforward to dissolve any bulk Cu either electrochemically or by rinsing with aerated aqueous H_2SO_4 to leave the PdCu core/shell particles behind as indicated in Fig. 6b/II.

Patterning of Pd/Cu layer. It has been reported in previous STM studies of Pd deposition on top of pyridine terminated SAMs[25, 31] that metal nanoparticles adhere very weakly to the SAM. The same also holds for the PdCu particles which combines favourably with the possibility to deposit them at high density as this offers the possibility of lithographic patterning and generating metallic nanostructures.

As illustrated in Figure 7a patterning was explored in two steps using both STM and AFM as patterning tools. In the first step particles are removed by bringing the tip sufficiently close to or in contact with the surface so that the interactions of the PdCu particles with the tip exceeds those between the particles and their adhesion to the SAM. The following second step exploits the deposition contrast between a native SAM which is electrochemically blocking, and a nanoparticle covered SAM which, as discussed above, behaves like a bulk electrode. In reversal of the dissolution of bulk Cu (see Fig. 6b) electrodeposition yields a pattern of an ultrathin continuous metal layer (step 3 of the scheme in Figure 7a). It is noted that the particle mediated, patterned electrodeposition is conceptually similar to a scheme where patterns of ligand stabilised Pd or Au nanoparticles were generated by displacement with an AFM and the catalytic activity of the particles exploited for electroless Ni plating.[71]

Figures 7b and 7c show two examples of particle removal by an STM tip. To remove particles, tunneling conditions were changed from imaging mode (0.5 V/3 pA) to higher currents and lower bias where transfer of the particle to the tip occurs (0.1 V/250 pA). The S-like pattern shown in Figure 7b was generated by a sequence of squares and rectangles in order of the numbers. The possibility of high resolution patterning is demonstrated in Figure 7c showing a line with sub-10 nm width.

The effect of deposition contrast between areas free of and covered by nanoparticles is demonstrated in Figure 7d. A sample is shown where PdCu nanoparticles were selectively removed employing an AFM (step 2 of Figure 7a) before subjected to conventional Cu deposition from the bulk electrolyte (step 3). Since metal layer and SAM interact only weakly, the images of Figure 7d were recorded in tapping mode using a Bruker Dimension Icon AFM, whereas patterning of a PdCu layer was performed in contact mode using a Nanosurf EasyScan2 instrument. Discussing the dependence of the process on the numerous experimental parameters comprising CuPd density, Cu electrolyte concentration and deposition potential and time in detail in a forthcoming publication, we only note here that in this proof of concept experiment a pulsed deposition protocol was applied to achieve both a uniform layer and a clear deposition contrast between particle covered and particle free areas. The clear deposition contrast between particle covered and free areas is clearly seen in the two images of Figure 7d. The deposition of bulk Cu is reflected in the height profile which shows a layer thickness of around 15 nm whereas the layer of PdCu particles (Figure

7b, c) has a thickness of 1-2 nm. Comparing the different areas where particles have been removed there is a variation in the suppression of Cu deposition. The large area in the upper half of the large scale image clearly shows some deposits whereas the narrow areas shown in the high magnification image exhibit excellent contrast. The difference can be ascribed to the difference in density of the scan lines which decreased from 5 nm to nominally 1.25 nm with decreasing width of the areas. This suggests that the deposits do not arise from a loss of contrast due to localised damage of the SAM but are the result of an incomplete removal of particles if the separation of the scan lines is too wide.

These images demonstrate, on the one hand, the potential of the patterning scheme for the generation of metal structures down to the ultra-small length scale. On the other hand, it also highlights the issues to be addressed for further improvement of resolution and accuracy. Featuring an average width of less than 10 nm, the line shown in Fig. 7c varies substantially which is no surprise considering the particle size distribution. As seen from Figure 4b particles vary in size from less than 2 nm to more than 5 nm, which also means variations in their connectivity, i.e. the forces they adhere to each other. As the patterning relies on the competition of interactions (tip particle vs particle-particle and particle-SAM) both factors are equally important. Therefore, the limit in resolution and accuracy is defined by the level of control over the distribution of particle size and location for which it will be crucial to understand the factors determining the nucleation process and how these correlate with the structure of the SAM.

CONCLUSION

The quality and structural stability of a SAM of a pyridine terminated aromatic-aliphatic thiol affords the electrochemical codeposition of metals, one from a 2D layer of ions coordinated at the SAM-electrolyte interface and another one from the bulk electrolyte. The characteristic feature of this coordination controlled deposition scheme is that, upon reduction and nucleation, the coordinated metal acts as a seed for deposition of the second metal, thus yielding bimetallic structures. Depending on deposition conditions these can range from isolated nanoparticles to ultrathin continuous layers, thus offering opportunities for branching out in different directions. Given the interest in bimetallic nanoparticles for (electro)catalysis,[72, 73] one is the exploration of how the structural and compositional degrees of freedom can be harnessed for tailoring reactivity and selectivity. As regards continuous layers, advancing the percolation threshold to ever thinner films, in combination with lateral patterning on the ultrasmall scale, is appealing for designing optical and electronic properties, in particular by making use of hybrid structures and the increasing influence of the metal-organic interface.[74-76]

Common to both nanoparticles and continuous layers central points to be addressed in future work are how size, structure and composition of the nanoparticles can be controlled and, in turn, (electro)chemical, optical and electronic properties of the deposits be tailored. Besides the obvious parameter space comprising different metals and variation of deposition parameters such as overpotential, and concentrations of coordinated and bulk metal species, a better understanding of the role of the SAM is also essential for two reasons. Firstly, the achievable resolution will ultimately be determined by the level of control over diffusion and nucleation of the metal species at the SAM/electrolyte interface. Calculations suggesting that diffusion is more complex than a simple site to site hopping on a pure SAM surface,[77, 78] it is unclear at present how these processes occur and what the influence of structural features of the SAM is such as surface corrugation or domain boundaries. Secondly, controlling adhesion between the deposit and SAM is important as, on the one hand, a good adhesion is desired when using the structures as deposited whereas, in extension of SAM templated electrodeposition,[12] an easy lift off is required to enable the transfer to insulating substrates in order to harness specific features of the metal structures like optical transparency and ultra-small lateral dimensions.

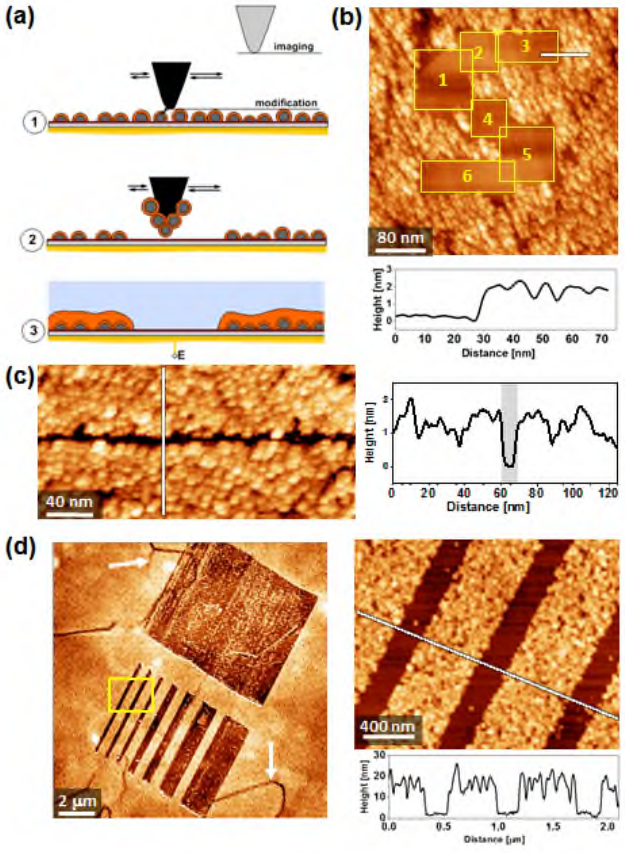

Figure 7. Scanning probe based patterning of CuPd layer deposited on top of PyP3 SAM by CCED. (a) Patterning scheme involving removal of CuPd particles by scanning probe (1,2) and subsequent selective electrodeposition (3). (b) STM image of CuPd layer patterned by a sequence of removal scans indicated by yellow quadrangles. White line marks location of height profile shown below. (c) Single line in CuPd layer written by STM. Height profile is along white line. Gray bar in the height profile marks the line of sub-10 nm width. (d) AFM patterning of CuPd layer and subsequent electrodeposition of Cu. Yellow rectangle in the large scale image on the left marks area of higher magnification image displayed on the right. Arrows in large image mark some of the boundaries between grains in the Au film. Experimental conditions: (b,c) Imaging 0.5 V/3 pA, modification 0.1 V/250 pA, deposition: as in Fig. 4 (d) Patterning parameters: force 42 nN, separation between scan lines varies from 5 nm (large area) to 1.25 nm (smallest feature), scan speed 2 lines/s. CuPd particles were generated by applying a pulse of -0.4 V (vs Cu^{2+}/Cu) for 0.1 s and dissolving any bulk Cu by immersion into sulfuric acid. For Cu deposition after patterning a sequence of 5 potential steps was applied consisting of -0.3 V/ 0.05 s deposition pulse, separated by a -0.05 s at a potential of 0.03 V. As electrolyte a 50 mM $CuSO_4$/50 mM H_2SO_4 solution was used for depositions before and after patterning.

AUTHOR INFORMATION

Corresponding Author

* E-mail: mb45@st-andrews.ac.uk. Phone: +44 (0)1334 467232

Present Addresses

† Department of Chemistry, Queen's University, 90 Bader Lane, Kingston, K7L 3N6, Canada

Notes

The authors declare no competing financial interest. The research data supporting this publication can be accessed at DOI: number will be added in proof corrections

Conflicts of Interest

There are no conflicts of interest to declare.

ACKNOWLEDGEMENTS

Support by EPSRC (EP/E061303/1, EP/D048761/1) and the Chinese Scholarship Council and the University of St Andrews for a stipend (Z.Y.) are gratefully acknowledged.

REFERENCES

1. A. Gölzhäuser and C. Wöll, *ChemPhysChem*, 2010, **11**, 3201-3213.
2. R. K. Smith, P. A. Lewis and P. S. Weiss, *Prog. Surf. Sci.*, 2004, **75**, 1-68.
3. J. J. Gooding and S. Ciampi, *Chem. Soc. Rev.*, 2011, **40**, 2704-2718.
4. D. Zabetakis and W. J. Dressick, *ACS Appl. Mater. Interfaces*, 2009, **1**, 4-25.
5. P. L. Schilardi, P. Dip, P. C. D. Claro, G. A. Benitez, M. H. Fonticelli, O. Azzaroni and R. C. Salvarezza, *Chem. Eur. J.*, 2005, **12**, 38-49.
6. M. Buck, in *Advances in Electrochemical Science and Engineering* eds. R. Alkire, D. M. Kolb, J. Lipkowski and P. N. Ross, Wiley-VCH, Weinheim, 2009, vol. 11, pp. 197-255
7. J. A. M. Sondag-Huethorst, H. R. J. Vanhelleputte and L. G. J. Fokkink, *Appl. Phys. Lett.*, 1994, **64**, 285-287.
8. O. Azzaroni, M. H. Fonticelli, G. Benitez, P. L. Schilardi, R. Gago, I. Caretti, L. Vazquez and R. C. Salvarezza, *Adv. Mater.*, 2004, **16**, 405-408.
9. P. L. Schilardi, O. Azzaroni and R. C. Salvarezza, *Langmuir*, 2001, **17**, 2748-2752.
10. T. Felgenhauer, C. Yan, W. Geyer, H. T. Rong, A. Gölzhäuser and M. Buck, *Appl. Phys. Lett.*, 2001, **79**, 3323-3325.
11. I. Thom, G. Hähner and M. Buck, *Appl. Phys. Lett.*, 2005, **87**.
12. Z. She, A. DiFalco, G. Hähner and M. Buck, *Beilst. J. Nanotechnol.*, 2012, **3**, 101-113.
13. Z. She, A. Di Falco, G. Hähner and M. Buck, *Appl. Surf. Sci.*, 2016, **373**, 51-60.
14. N. S. Pesika, A. Radisic, K. J. Stebe and P. C. Searson, *Nano Lett.*, 2006, **6**, 1023-1026.
15. N. S. Pesika, F. Q. Fan, P. C. Searson and K. J. Stebe, *J. Am. Chem. Soc.*, 2005, **127**, 11960-11962.
16. G. Pattanaik, W. Shao, N. Swami and G. Zangari, *Langmuir*, 2009, **25**, 5031-5038.
17. M. A. Schneeweiss, H. Hagenstrom, M. J. Esplandiu and D. M. Kolb, *Appl. Phys. A-Mater. Sci. Process.*, 1999, **69**, 537-551.
18. C. Shen and M. Buck, *Beilst. J. Nanotechnol.*, 2014, **5**, 258-267.
19. A. Turchanin and A. Gölzhäuser, *Prog. Surf. Sci.*, 2012, **87**, 108-162.
20. G. Kaltenpoth, B. Völkel, C. T. Nottbohm, A. Gölzhäuser and M. Buck, *J. Vac. Sci. Technol. B*, 2002, **20**, 2734-2738.
21. B. Völkel, G. Kaltenpoth, M. Handrea, M. Sahre, C. T. Nottbohm, A. Küller, A. Paul, W. Kautek, W. Eck and A. Gölzhäuser, *Surf. Sci.*, 2005, **597**, 32-41.
22. W. J. Dressick, C. S. Dulcey, J. H. Georger, G. S. Calabrese and J. M. Calvert, *J. Electrochem. Soc.*, 1994, **141**, 210-220.
23. H. Kind, A. M. Bittner, O. Cavalleri, K. Kern and T. Greber, *J. Phys. Chem. B*, 1998, **102**, 7582-7589.
24. K. Uosaki, H. Fukumitsu, T. Masuda and D. Qu, *Phys. Chem. Chem. Phys.*, 2014, **16**, 9960-9965.
25. M. I. Muglali, A. Bashir, A. Birkner and M. Rohwerder, *J. Mater. Chem.*, 2012, **22**, 14337-14340.
26. T. Baunach, V. Ivanova, D. M. Kolb, H. G. Boyen, P. Ziemann, M. Buttner and P. Oelhafen, *Adv. Mater.*, 2004, **16**, 2024-2028.
27. D. Y. Qu, M. Ito, H. Noguchi and K. Uosaki, *Chem. Lett.*, 2010, **39**, 110-111.
28. D. Y. Qu and K. Uosaki, *Chem. Lett.*, 2006, **35**, 258-259.
29. D. Qu and K. Uosaki, *J. Phys. Chem. B*, 2006, **110**, 17570-17577.
30. O. Shekhah, C. Busse, A. Bashir, F. Turcu, X. Yin, P. Cyganik, A. Birkner, W. Schuhmann and C. Woll, *Phys. Chem. Chem. Phys.*, 2006, **8**, 3375-3378.
31. C. Silien, D. Lahaye, M. Caffio, R. Schaub, N. R. Champness and M. Buck, *Langmuir*, 2011, **27**, 2567-2574.
32. F. Eberle, M. Metzler, D. M. Kolb, M. Saitner, P. Wagner and H. G. Boyen, *ChemPhysChem*, 2010, **11**, 2951-2956.
33. M. Manolova, M. Kayser, D. M. Kolb, H. G. Boyen, P. Ziemann, D. Mayer and A. Wirth, *Electrochim. Acta*, 2007, **52**, 2740-2745.
34. V. Ivanova, M. Manolova and D. M. Kolb, in *Nanoscience and Technology, Pts 1 and 2*, eds. C. Bai, S. Xie and X. Zhu, 2007, vol. 121-123, pp. 363-367.
35. H. G. Boyen, P. Ziemann, U. Wiedwald, V. Ivanova, D. M. Kolb, S. Sakong, A. Gross, A. Romanyuk, M. Buttner and P. Oelhafen, *Nature Mat.*, 2006, **5**, 394-399.
36. M. Manolova, V. Ivanova, D. M. Kolb, H. G. Boyen, P. Ziemann, M. Buttner, A. Romanyuk and P. Oelhafen, *Surf. Sci.*, 2005, **590**, 146-153.
37. V. Ivanova, T. Baunach and D. A. Kolb, *Electrochim. Acta*, 2005, **50**, 4283-4288.
38. F. Eberle, M. Saitner, H. G. Boyen, J. Kucera, A. Gross, A. Romanyuk, P. Oelhafen, M. D'Olieslaeger, M. Manolova and D. M. Kolb, *Angew. Chem. Int. Ed.*, 2010, **49**, 341-345.
39. D. Qu and K. Uosaki, *J. Electroanal. Chem.*, 2011, **662**, 80-86.
40. M. I. Muglali, J. Liu, A. Bashir, D. Borissov, M. Xu, Y. Wang, C. Woell and M. Rohwerder, *Phys. Chem. Chem. Phys.*, 2012, **14**, 4703-4712.
41. L. Herrer, V. Sebastian, S. Martin, A. Gonzalez-Orive, F. Perez-Murano, P. J. Low, J. L. Serrano, J. Santamaria and P. Cea, *Nanoscale*, 2017, **9**, 13281-13290.
42. H. Müller, M. Metzler, N. Barth, B. Conings, H. G. Boyen, T. Jacob and L. Kibler, *Electrocatalysis*, 2018, **9**, 505-513.
43. H. L. Lin, J. M. Yang, J. Y. Liu, Y. F. Huang, J. L. Xiao and X. Zhang, *Electrochim. Acta*, 2013, **90**, 382-392.
44. G. Gao, D. Guo, C. Wang and H. Li, *Electrochem. Commun.*, 2007, **9**, 1582-1586.
45. D. J. Guo and H. L. Li, *Electrochem. Commun.*, 2004, **6**, 999-1003.
46. H.-T. Rong, S. Frey, Y.-J. Yang, M. Zharnikov, M. Buck, M. Wühn, C. Wöll and G. Helmchen, *Langmuir*, 2001, **17**, 1582-1593.
47. P. Cyganik, M. Buck, J. D. E. T. Wilton-Ely and C. Wöll, *J. Phys. Chem. B*, 2005, **109**, 10902-10908.
48. C. Silien, M. Buck, G. Goretzki, D. Lahaye, N. R. Champness, T. Weidner and M. Zharnikov, *Langmuir*, 2009, **25**, 959-967.
49. H. Hagenstrom, M. A. Schneeweiss and D. M. Kolb, *Langmuir*, 1999, **15**, 7802-7809.
50. I. Horcas, R. Fernandez, J. M. Gomez-Rodriguez, J. Colchero, J. Gomez-Herrero and A. M. Baro, *Rev. Sci. Instrum.*, 2007, **78**.
51. J. F. Moulder, W. F. Stickle, P. E. Sobol and K. E. Bomben, *Handbook of X-ray Photoelectron Spectroscopy*, Perkin Elmer Corporation, 1992.
52. G. Kumar, J. R. Blackburn, R. G. Albridge, W. E. Moddeman and M. M. Jones, *Inorg. Chem.*, 1972, **11**, 296-300.

53. J. Poppenberg, S. Richter, E. Darlatt, C. H. H. Traulsen, H. Min, W. E. S. Unger and C. A. Schalley, *Surf. Sci.*, 2012, **606**, 367-377.
54. R. Nyholm, N. Martensson, A. Lebugle and U. Axelsson, *J. Phys. F: Metal Phys.*, 1981, **11**, 1727.
55. Y. Zubavichus, M. Zharnikov, Y. Yang, O. Fuchs, E. Umbach, C. Heske, A. Ulman and M. Grunze, *Langmuir*, 2004, **20**, 11022-11029.
56. N. Wattanavichean, M. Gilby, R. J. Nichols and H. Arnolds, *Anal. Chem.*, 2019, **91**, 2644-2651.
57. J. Kucera and A. Gross, *Phys. Chem. Chem. Phys.*, 2012, **14**, 2353-2361.
58. L. Mattarozzi, S. Cattarin, N. Comisso, R. Gerbasi, P. Guerriero, M. Musiani and E. Verlato, *Electrochim. Acta*, 2017, **230**, 365-372.
59. Q. Dong, Y. Zhao, X. Han, Y. Wang, M. Liu and Y. Li, *Int. J. Hydrogen Energy*, 2014, **39**, 14669-14679.
60. W. P. Zhou, T. Baunach, V. Ivanova and D. M. Kolb, *Langmuir*, 2004, **20**, 4590-4595.
61. J.-L. Lin, C.-H. Ye, B.-C. Lin, S.-H. Li, Z.-X. Yang, Y.-H. Chiang, S.-W. Chen, C.-H. Wang, Y.-W. Yang and J.-C. Lin, *J. Phys. Chem. C*, 2015, **119**, 26471-26480.
62. M. R. Cohen and R. P. Merrill, *Langmuir*, 1990, **6**, 1282-1288.
63. C. Wockel, A. Eilert, M. Welke, M. Schoppke, H. P. Steinruck and R. Denecke, *J. Chem. Phys.*, 2016, **144**.
64. C. Milhano and D. Pletcher, *J. Electroanal. Chem.*, 2008, **614**, 24-30.
65. D. Reyter, D. Bélanger and L. Roué, *J. Phys. Chem. C*, 2009, **113**, 290-297.
66. J.-N. Chazalviel and P. Allongue, *J. Am. Chem. Soc.*, 2011, **133**, 762-764.
67. V. García-Morales and K. Krischer, *Proc. Natl. Acad. Sci.*, 2010, **107**, 4528.
68. O. Y. Sliusarenko, A. I. Oleinick, I. B. Svir and C. A. Amatore, *Russ. J. Electrochem.*, 2017, **53**, 1019-1028.
69. Y. Negishi, T. Nakazaki, S. Malola, S. Takano, Y. Niihori, W. Kurashige, S. Yamazoe, T. Tsukuda and H. Häkkinen, *J. Am. Chem. Soc.*, 2015, **137**, 1206-1212.
70. M. M. Alvarez, J. T. Khoury, T. G. Schaaff, M. N. Shafigullin, I. Vezmar and R. L. Whetten, *J. Phys. Chem. B*, 1997, **101**, 3706-3712.
71. S. L. Brandow, W. J. Dressick, C. S. Dulcey, T. S. Koloski, L. M. Shirey, J. Schmidt and J. M. Calvert, *J. Vac. Sci. Technol. B*, 1997, **15**, 1818-1824.
72. S. E. F. Kleijn, S. C. S. Lai, M. T. M. Koper and P. R. Unwin, *Angew. Chem. Int. Ed.*, 2014, **53**, 3558-3586.
73. J. T. L. Gamler, H. M. Ashberry, S. E. Skrabalak and K. M. Koczkur, *Adv. Mater.*, 2018, **30**.
74. F. A. Ma'Mari, T. Moorsom, G. Teobaldi, W. Deacon, T. Prokscha, H. Luetkens, S. Lee, G. E. Sterbinsky, D. A. Arena, D. A. MacLaren, M. Flokstra, M. Ali, M. C. Wheeler, G. Burnell, B. J. Hickey and O. Cespedes, *Nature*, 2015, **524**, 69-73.
75. H.-T. Chen, A. J. Taylor and N. Yu, *Rep. Prog. Phys.*, 2016, **79**, 076401.
76. C. Zhang, N. Kinsey, L. Chen, C. Ji, M. Xu, M. Ferrera, X. Pan, V. M. Shalaev, A. Boltasseva and L. J. Guo, *Adv. Mater.*, 2017, **29**, 1605177.
77. J. A. Keith and T. Jacob, *Chem. Eur. J.*, 2010, **16**, 12381-12386.
78. J. A. Keith and T. Jacob, *Electrochim. Acta*, 2010, **55**, 8258-8262.